Optical transition radiation based transverse beam diagnostics for nonrelativistic ion beams

R. Singh[*], T. Reichert, and B. Walasek-Hoehne

GSI, Planckstraße 1, 64291 Darmstadt, Germany

The usage of optical transition radiation (OTR) for profile monitoring of relativistic electron beams is well known. This paper presents the case for beam diagnostic application of OTR for nonrelativistic ion beams. In addition to expected linearly polarized transition radiation in the plane of observation, a significant component of observed radiation is unpolarized. The unpolarized contribution increases as the target is tilted toward the grazing angles with its intensity, an order of magnitude higher than the polarized radiation. This unpolarized radiation is shown to have the characteristics of OTR and is qualitatively explained as the OTR generated on a rough target surface. This increase in observed radiation can be used advantageously for transverse profile measurements. Further systematic effects such as the dependence of light yield on beam current, comparison of the measured transverse profiles with secondary electron emission based grid, target heating, and prompt nature of observed radiation are reported.

I. INTRODUCTION

Transition radiation (TR) is generated over a wide frequency range when a charged particle traverses two different media. The existence of TR was first predicted by Ginzburg and Frank [1] where the expressions for the radiation intensity of the far field angular distribution were derived. The radiation intensity is typically evaluated between two homogeneous media with different permittivities such as the vacuum-metal boundary which is often the case for most practical realizations.

A common picture for visualizing transition radiation in the case of a planar vacuum-metal interface is the following: As the charged particle approaches the interface from the vacuum side, the Coulomb fields associated with the charge are terminated on the metal such that the boundary conditions are satisfied by the induced polarization. However, when the charge hits the metal vacuum-metal interface, the boundary conditions can only be satisfied with the addition of radiating electromagnetic fields which are referred to as transition radiation [2]. A similar process occurs upon the emergence of the charged particle on the other side of the metal-vacuum interface. The emitted radiation is often separated as backward transition radiation (BTR) when the emission is in the first medium and

forward transition radiation (FTR) when it is observed in the second medium. For nonrelativistic ion beams, the beam is typically deposited within the first few micrometers from the target surface and there is no forward transition radiation expected unless very thin foils are used. One has to note that although simple descriptions for transition radiation are given for the vacuum-metal interface, transition radiation occurs at every material interface or while traversing an inhomogeneous medium. With respect to the temporal extent of particle bunches, another distinction commonly used in the jargon of transition radiation is coherent vs incoherent transition radiation. The radiation is referred to as coherent if the observed wavelength is comparable to the size of the source's charge distribution. Coherent transition radiation for optical frequencies would only occur for bunches with temporal lengths in the order of a few femtoseconds (fs). In the next section, the expression for OTR from a smooth target surface on ion beam irradiation is presented. Then a qualitative model of the rough target surface and expected modifications in OTR are discussed. In the following sections, experimental setup, results, and applications are presented.

II. MODELING ASPECTS

Figure 1 shows the schematic of the particle trajectory, a target or radiator and the detector which is typically a charge-coupled device (CCD) based camera, along with the relevant symbols. The coordinate system is chosen in-line with [3], i.e., the OTR target plane is defined as the *x-y* plane and the target normal is toward the *z* axis. The *plane of incidence* consists of target normal $\vec{n}$ and beam incidence vector $\vec{\beta}$ and the angle between these planes

is referred to as the irradiation angle (ψ). The plane of incidence coincides with the x-z plane in the shown schematic. The *plane of radiation* consists of $\vec{n}$ and radiation wavevector $\vec{k}_{\mathrm{BTR}}$ while the *plane of observation* contains beam incidence vector $\vec{\beta}$ and the detector position $\vec{n}_{\mathrm{det}}$. The beam incidence, target normal, and detector position vectors are all in the same plane in our experimental setup, i.e., the plane of incidence and plane of observation coincide. Further, since only the radiation in the plane of observation is detected due to a small acceptance of the detector (i.e., $\frac{\vec{k}_{\mathrm{BTR}}}{|\vec{k}_{\mathrm{BTR}}|} \approx \vec{n}_{\mathrm{det}}$), the relevant radiation vector also lies in the same plane as incidence and observation, i.e., x-z plane.

A. Optical transition radiation from smooth target

Ideal surfaces where the structures on the surface are much smaller than the wavelength of interest ($\ll \lambda$) are loosely referred to as smooth surfaces. For smooth surfaces, the direction of the target surface normal is not a function of the exact location on the target surface. If an ion beam with a charge state Z is traversing from the vacuum (medium 1) with $\epsilon_1 = 1$ into a smooth target (medium 2) with a relative permittivity $\epsilon_2 = \epsilon$ at an irradiation angle ψ, the angular distribution of the far field intensity with a polarization parallel to plane of radiation (p polarized) as a function of irradiation angle and emission angle θ is given as [3],

$$\frac{dI_{\parallel}(n, \omega, \theta, \phi, \psi)}{d\Omega d\omega} = \frac{Z^2 e^2 \beta_z^2 \cot^2\theta |\epsilon - 1|^2}{4\pi^3 \epsilon_0 c[(1 - \beta_x \cos\theta_x)^2 - \beta_z^2 \cos^2\theta]^2} \|A\|^2, \tag{1}$$

where,

$$A = \frac{(1 + \beta_z \sqrt{\epsilon - \sin^2\theta} - \beta_z^2 - \beta_x \cos\theta_x)\sin^2\theta - \beta_x \beta_z \cos\theta_x \sqrt{\epsilon - \sin^2\theta}}{(\epsilon \cos\theta + \sqrt{\epsilon - \sin^2\theta})(1 - \beta_x \cos\theta_x + \beta_z \sqrt{\epsilon - \sin^2\theta})} \tag{2}$$

and, $\beta_x = \beta \sin\psi$, $\beta_z = \beta \cos\psi$ and $\cos\theta_x = \sin\theta \cos\phi$.

There is also a component polarized perpendicular to the plane of radiation (s-polarized) $I_{\perp}$, however $I_{\perp} \approx I_{\parallel} \cdot \beta^4$ It is thus expected to be negligible in comparison to parallel components for kinetic energies relevant to our studies where $\beta < 0.3$. The charge square dependence of OTR signal intensity makes OTR a viable diagnostic mechanism for heavy ion beams. For smooth targets oriented as shown in Fig. 1, we expect the radiation detected by the camera to be linearly polarized since the target normal ($\vec{n}$) lies in the plane of observation.
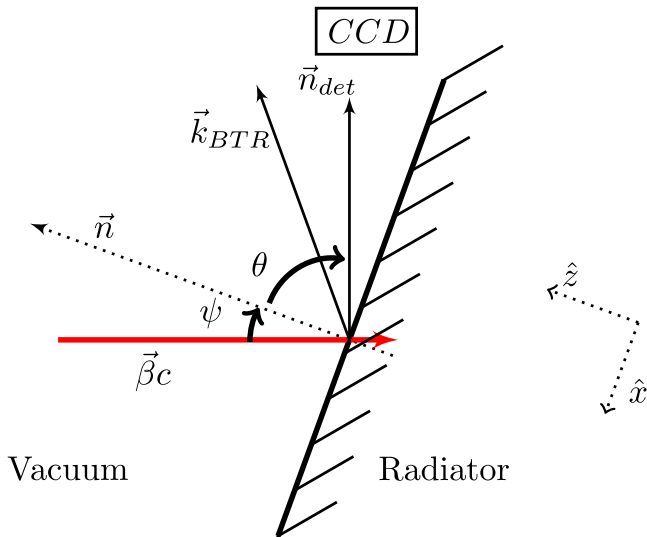
Figure 2(a) shows a polar diagram representing the angular distribution given by Eq. (1) for a unit charge with velocity $\beta = 0.15$ incident normally on a perfect electrical conductor (PEC) and a realistic conductor, i.e., iron (Fe). Here the relative permittivity of iron at 500 nm was used [4]. The peak of the radiation for an iron target is at $\theta \approx 60°$ irrespective of the angle of irradiation ψ while for PEC, it is $\psi = 90°$. Figure 2(b) shows the angular distribution for various irradiation angles. The cumulative spectral intensity is highest for the case of normal incidence onto the target.

Optical transition radiation from low energy electron beams has been already observed and utilized at several facilities [5,6]. For low energy hadron beams, usage of OTR for diagnostic purposes was proposed due to potential signal increase due to ion charge state [7]. Following this, some pilot measurements were done, which confirmed the charge state dependency of light yield and prompt nature of the signal [8]. Spectroscopic investigations showed broadband radiation indicating the presence of OTR and were first reported in [9]. Polarization, angular dependence, and light yield were not studied in that contribution. Since the charge state dependency also exists for other competing light producing mechanisms like beam induced fluorescence (BIF), the data did not conclusively confirm the measured radiation as OTR in those pilot studies. Our measurements fill some of those gaps.

FIG. 1.   Charged particle beam impinging on a metal target.

B. Optical transition radiation from a rough target

The targets used in this study were not controlled for surface roughness and had pre-irradiation surface roughness factor R_a in the range of 0.06–0.25 μm. The surface
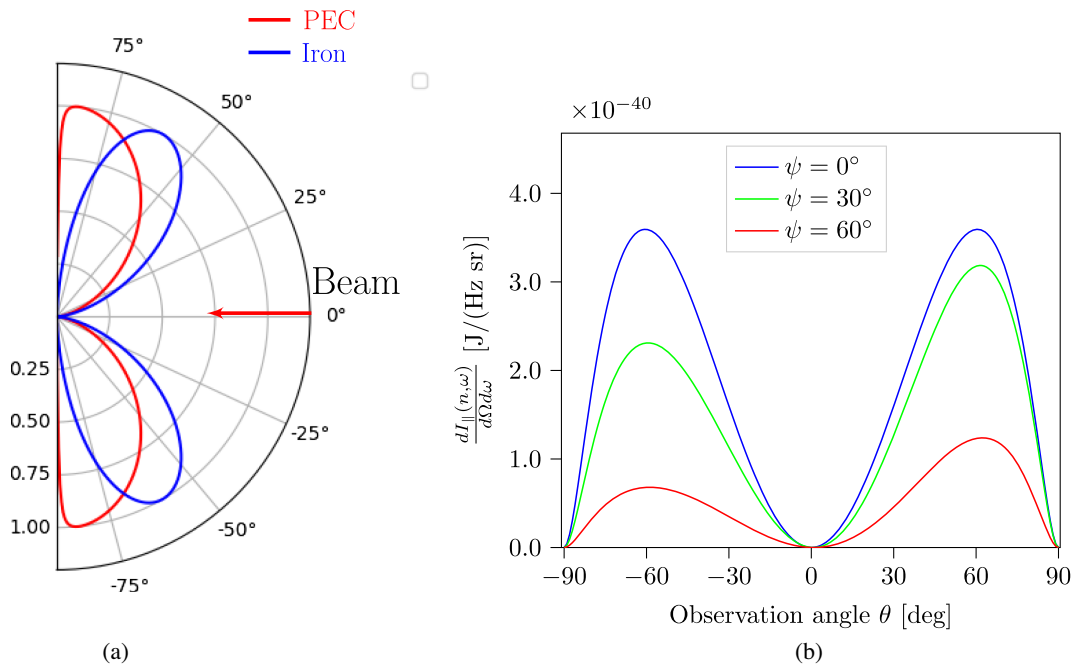
FIG. 2. (a) Polar plot showing the angular distribution of transition radiation emission from an iron target in comparison to perfect electric conductor (PEC) when irradiated by a singly charged particle with velocity $\beta = 0.15$ at $\psi = 0°$. (b) The angular distribution of intensity for an iron target when irradiated at different angles.

roughness factor R_a is defined as the arithmetic mean of the departure of the profile from a mean line $R_a = \frac{1}{L} \int_0^L |y(x)| dx$, where $y(x)$ is the surface height with respect to mean line at the location x on a line of length L. The energy deposition due to the ion bombardment degrades the surface for the energy and intensity regime used in our study after a short period of irradiation. The roughness is at least increased by a factor of 5 after irradiation (see Appendix D). In literature, rough surfaces are typically characterized as "weak" or "strong" rough surfaces based on the surface roughness factor and correlation length in comparison to the relevant radiation wavelength [10]. An important concept for transition radiation generation is the "effective source size" r_{eff}, which for a given radiation wavelength λ and beam velocity βc is given as $\beta\gamma\lambda/2\pi$ [11,12]. Further, it is also important to note that for $\beta < 0.5$, it is not possible to control target roughness on the scale of effective source size for optical wavelengths under heavy ion irradiation. Thus, for the radiation emitted in the optical regime, the effective source size is smaller than the surface roughness factor, i.e., $R_a/r_{eff} \gg 10$. Therefore, all the target surfaces utilized in our study can be considered "strongly rough." Each structure on the rough surface has the possibility to act as an individual "microradiator" for transition and diffraction radiation with its own target normal which may not coincide with plane of observation. This in turn means that the OTR characteristics can change drastically since the target normal varies locally across the whole target depending on the specific structure of the target surface at that location and produces a distribution of

angles between plane of radiation and the plane of observation. Another related concept in transition radiation is the so-called formation zone [13,14] and is given by $L_{formation} = \frac{\lambda\beta\sqrt{\epsilon_0}}{2\pi(1-\beta\sqrt{\epsilon_0}\cos\theta)}$, where ϵ_0 is given as $(\epsilon_1 + \epsilon_2)/2$. One should note that in the context of rough surfaces, the definition of formation zone is a bit modified from the original derivation [15]. Since the formation zone is comparable to the wavelength for low energy ion beams as well as the roughness of the target, the angular distribution of generated radiation can be modified [12], unlike the typically considered cases of smooth targets and higher energy beams ($\gamma \gg 1$).

Figure 3 shows a schematic of a rough target surface consisting of piecewise planar microsurfaces. The proportion of the polarized light measured in the plane of observation will be given by the relative distribution of microscopic target normals $\vec{n}_{micro}$ of individual radiators with respect to the macroscopic target normal $\vec{n}_{macro}$ which was earlier simply denoted as $\vec{n}$ as shown in Fig. 1. Here we assume that the target normals for individual microradiators are randomly distributed in the 2D angular space with respect to $\vec{n}_{macro}$ and have no preferred direction, i.e., $\vec{n}_{micro}$ is a random variable with respect to θ, ϕ with $\mathbf{E}[\vec{n}_{micro}] = \vec{n}_{macro}$ where $\mathbf{E}[]$ is the expectation operator. However, only the subset of microradiators normals $(\vec{n}_{micro,OTR})$ can contribute to OTR generation, i.e., the ones which can be directly irradiated by the beam. The red blob depicts the charged particle along with the field extent representing the effective source size for any given wavelength. A further complexity for transition radiation produced by low beta
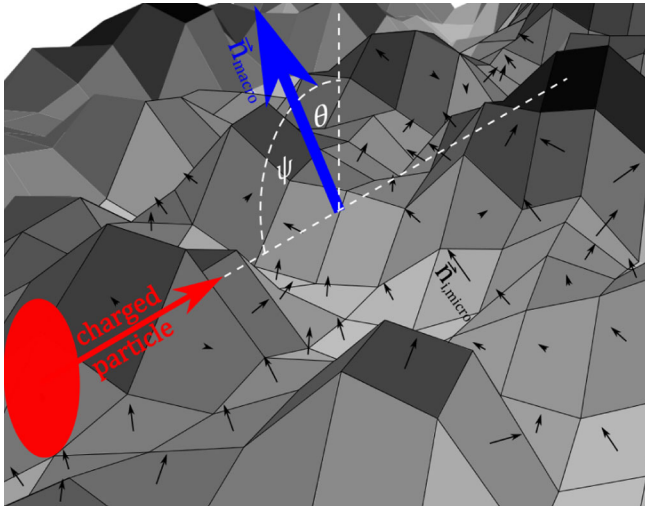
FIG. 3. Schematic representation of a target with a rough surface hit by a charged particle under shallow incidence. Given the depicted piecewise planar microsurfaces (with individual normals $\vec{n}_{i,\text{micro}}$) are bigger than the effective transversal extent of the incident electric field ($r_{\text{eff}} = \beta\gamma\lambda$ in vacuum), they can be thought as individual OTR sources.

beams arises from the fact that most radiation generated is directed perpendicular to the target normal (as shown in Fig. 2). This radiation can undergo scattering from the rough target surface before reaching the detector. The combined effect of randomly distributed radiator angles and surface scattering especially with a strong surface roughness has been used to interpret the polarization in the plane of observation as well as the angular distribution in the experimental section.

There has been early theoretical [13] and experimental [16] work showing differences in optical transition radiation photon yield and polarization for low energy electron beams arising from rough surfaces. These studies performed were mainly concerned with extremely shallow/grazing irradiation angles $\psi > 80°$. Observations similar to ours were made, i.e., an increase in light output at these grazing angles was also observed and assigned to diffraction radiation. Some studies with OTR and rough surfaces were performed to diffuse the radiation over a larger emission angle with 95 MeV electron beams [17]. More literature for low energy electron irradiation on metal targets is available where an increase in radiation at grazing angles irradiation is reported. However, these studies attribute the increase in radiation to the excitation of surface plasmons [18] or surface bremsstrahlung [19]. Surface bremsstrahlung is not relevant for ion irradiation studies. It is also known from the literature that scattering via surface plasmons or surface polaritons is not expected to play any role for strongly rough metal targets and nonmetallic targets [10]. Nevertheless, we have utilized a nonmetallic OTR radiator to ascertain the potential contribution of surface plasmons in the detected radiation.

III. EXPERIMENTAL ASPECTS AND RESULTS

The results presented in this paper were obtained in the X2 beamline downstream of the universal linear accelerator (UNILAC) at GSI. Most of the ion species are available depending on the user request with kinetic energies up to 11.4 MeV/u and beam currents up to few mAs. The ions are available in macropulses of up to 1 ms under 20 Hz operation. Further details can be found in [20]. Our experiments were performed with any available ion species in a *parasitic user* mode in parallel to the main user experiments. The experimental setup is shown in Fig. 4. The metal targets used were 35 mm wide and 100 mm high. Three metals were used: aluminum, stainless steel, and gold, where the former two were solid materials of 2 mm thickness and the latter was in form of a 1 μm thick layer sputtered on a 2-mm thick stainless steel holder. Another target was a 5-mm thick disc (of diameter 110 mm) made of glassy carbon. All of them were attached to a target ladder with a stepper motor based translation stage. A rotational stage was added to the ladder during the experiments, and therefore the absolute angle of the rotational element could not be precisely calibrated. On the acquisition side, a 10-mm objective with a 35-mm focal length was placed roughly 36 ± 3 cm above the target outside the vacuum using a custom holder marked as "camera system" in Fig. 4. Thus the optical system covers a solid angle $\Delta\Omega \approx 6 \times 10^{-4}$ Sr. A linear polarizer was mounted directly in front of the objective. The objective is followed by an image intensifier (Proxitronic, Image intensifier BV 2582 TX-V 100 N), which was fiber coupled to a BASLER CCD camera. The residual gas pressure in the vacuum chamber was measured to be about 5×10^{-7} mbar.

A. Expected number of photons in the detector

An estimate of the total number of photons expected from the backward transition radiation process in the
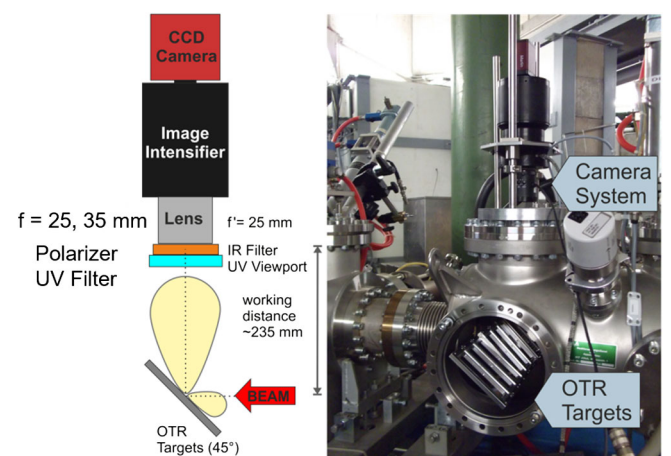

FIG. 4. The experimental setup showing the OTR target ladder mounted with several OTR targets and the optical system [9].
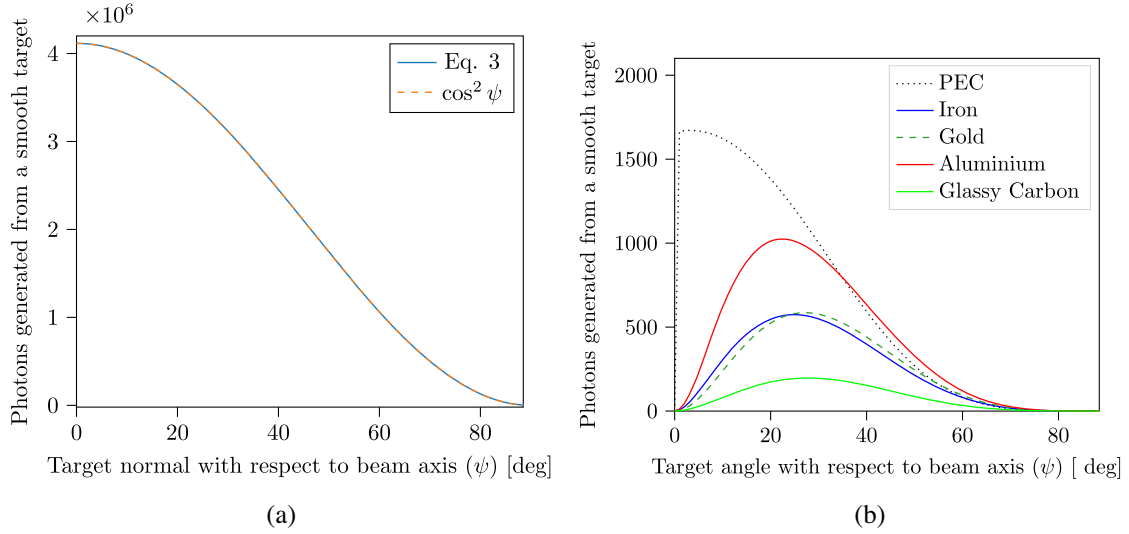
FIG. 5. (a) Total number of photons generated in $\Delta\lambda = 300$ nm with center at 500 nm in the half sphere as a function of ψ for 5×10^9 Ca^{10+} ions. (b) Expected number of photons in 6×10^{-4} sr from various target materials as a function of beam incidence with respect to normal (ψ) at the observation angle $\theta = 90° - \psi$.

backward half-space is discussed first. For a particle with a given charge state Z and velocity β, the total energy radiated in the frequency range of interest $\Delta\omega = \omega_2 - \omega_1$ and a half unit sphere on one side of the target can be obtained by integrating the radiation intensity given in Eq. (1).

$$E_{\rm rad} = \int_0^{\frac{\pi}{2}} \int_0^{2\pi} \int_{\omega_1}^{\omega_2} \frac{d^2 I_\parallel(n,\omega)}{d\Omega d\omega} \cdot \sin\theta d\theta d\phi d\omega. \quad (3)$$

Assuming that the frequency dependence of permittivity does not significantly alter the generated photon intensity (validity of this assumption is discussed in Appendix B) over the given frequency range and using the photon energy $E_{\rm ph} = \hbar\omega$ and the number of photons per particle is approximated by

$$
\begin{aligned}
N_{ph,t} &= \int_0^{\frac{\pi}{2}} \int_0^{2\pi} \int_{\omega_1}^{\omega_2} \frac{\frac{d^2 I_\parallel(n,\omega)}{d\Omega d\omega}}{E_{ph}} \sin\theta d\theta d\phi d\omega \\
&= \frac{\ln\left(\frac{\omega_2}{\omega_1}\right)}{\hbar} \int_0^{\frac{\pi}{2}} \int_0^{2\pi} \frac{d^2 I_\parallel(n,\omega)}{d\Omega d\omega} \sin\theta d\theta d\phi. \quad (4)
\end{aligned}
$$

Let us consider an example case of Ca^{10+} beam with energy corresponding to $\beta = 0.11$ and an average current of $40~\mu$A with $200~\mu$s macropulse length which in turn corresponds to $N_{\rm ion} = 5 \times 10^9$ ions per beam pulse. As the spatial pulse length is much longer than the detected wavelengths, we can scale Eq. (3) linearly with $N_{\rm ion}$ (incoherent sum) to find the total number of OTR photons generated by the described macropulse normally incident on a steel target as $\approx 4 \times 10^6$ photons. Due to the unavailability of steel permittivity values, iron permittivity is used for the calculation and it is assumed that the

wavelength range of acceptance of the optical system is centered at 500 nm wavelength with $\Delta\lambda = 300$ nm. Figure 5(a) shows the total photons generated as a function of beam incidence. A rough estimate of the total number of photons as a function of incident ion number $N_{\rm ions}$, energy, and charge state impinging at an angle ψ with respect to normal on a steel target can be given as

$$N_{ph,t} \approx 7 \times 10^{-4} \cdot \beta^2 Z^2 \cos^2\psi N_{\rm ions}. \quad (5)$$

The number of photons which will make into the optical system with a solid angle $\Delta\Omega = 0.0006$ sr as a function of beam incidence is shown in Fig. 5(b). Equation (4) and Fig. 5 are only valid for smooth targets. The transition from the well defined transition radiation generation process with a given polarization and angular distribution for a smooth surface to an apparently unpolarized source is governed by the surface roughness property and its interplay with the angle of incidence ψ as discussed in the previous section and depicted in Fig. 3. Generally, the dependency of light yield from a rough surface will differ from the qualitative picture discussed above for the smooth surface and depend on the shape of individual radiators as well as their distribution and separation. An accurate analysis requires a careful surface characterization and statistical analysis which we deem outside the scope of this work. We will only evaluate the dependency empirically in light of the above arguments later in this section.

B. Profile measurements from various targets

Figure 6 shows the two-dimensional beam images from the transition radiation for three target materials, aluminum, steel (V2A), and glassy carbon under the same beam and acquisition conditions. About 5×10^9 Ca^{10+} ions were
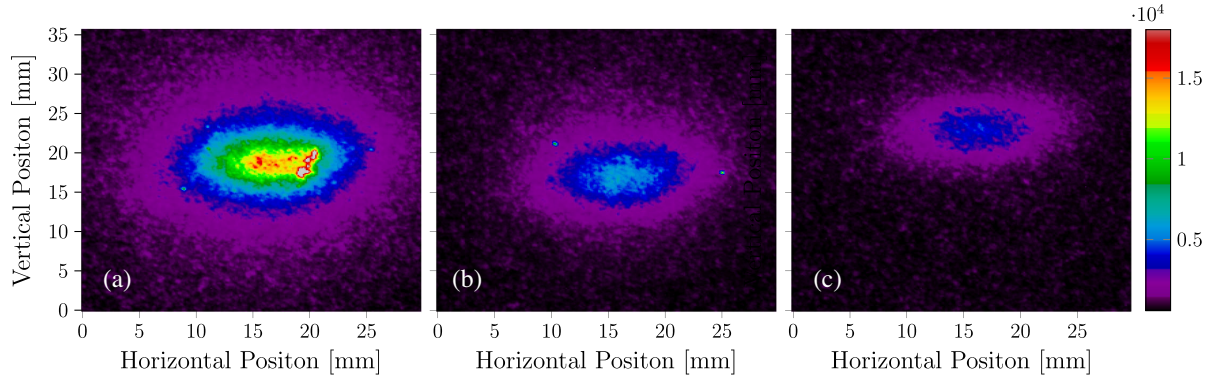
FIG. 6.   Transverse profile for aluminum (a), steel (b), and glassy carbon (c) targets for same beam conditions corresponding to $\psi = 50°$ for 5×10^9 Ca^{10+} ions per macropulse. The plot is an average of 250 macropulses in stable low intensity machine conditions.

irradiated on the targets at an irradiation angle of $\psi = 40°$. An average of over 250 images was performed to obtain the two-dimensional images where the color bars are fixed to same values for all of the three images. The photon count scaling trend for different target materials is similar to Fig. 5 and is also visible in the profile heights of the horizontal projection plotted in Fig. 7. The discrepancy is mainly for the steel target where we have used permittivity values for iron. We also see, that there is a saturated region on the aluminum target at the coordinates (20 mm, 20 mm; Fig. 6) and could be related to macroscopic surface structure on the target. Similar less pronounced spots are seen at (10 mm, 22 mm) and (25 mm, 17 mm) on the steel target. The measured profile width (FWHM) is 11.4, 11.2, and 10.2 mm for aluminum, steel, and glassy carbon targets, respectively. Although the glassy carbon has the lowest signal, the profile is the cleanest and should accurately represent the beam profile. Another observation is that the background is proportional to the peak height,
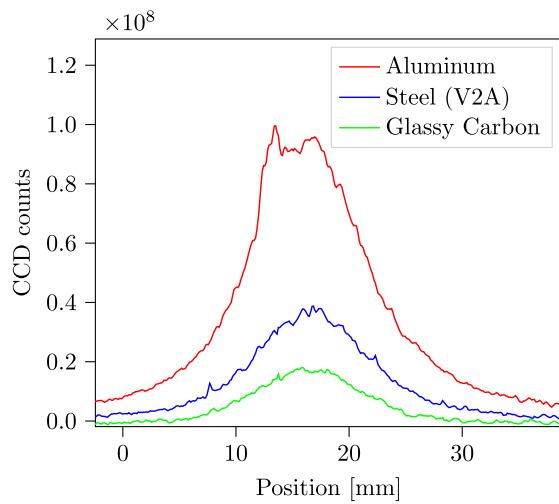
which hints that the background might be primarily composed of scattered OTR photons.

The CCD count itself is a strongly nonlinear function of intensifier voltage and cannot be directly correlated with the number of detected photons. However, for multiple measurements under the same beam conditions, the CCD count fluctuation can provide an estimate of the average number of photons generated. This is discussed further in Appendix A.

C. CCD counts vs beam current

A systematic study to observe the relation between average beam current against the number of counts for the same intensifier and CCD settings. This study was performed with a gold target with a bismuth Bi^{26+} beam. Figure 8 shows a single image of a 200-μA beam current at $\psi = 70$ deg. The background counts are subtracted by

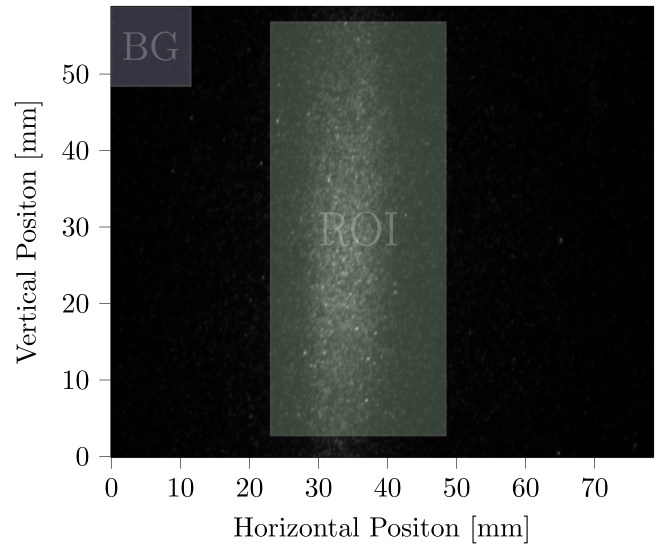FIG. 7.   Beam profile in horizontal plane for aluminum, steel, and glassy carbon targets for $\psi = 50$ degrees for 5×10^9 Ca^{10+} ions.

FIG. 8.   Individual image taken with an 80-μs gate for 200 μA Bi^{26+} beam current. The rectangle marked on the top left is used to subtract the background counts per pixel.
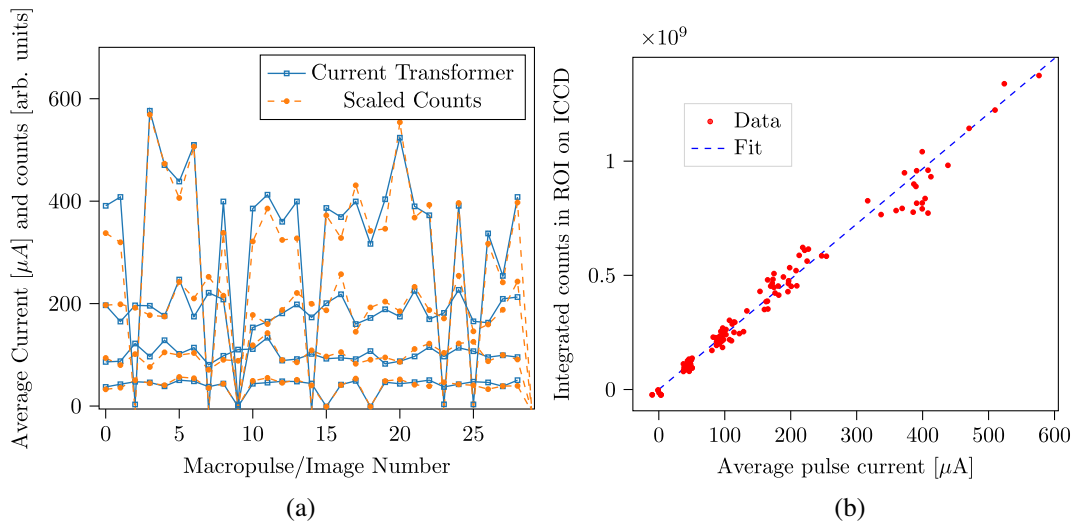
FIG. 9.   (a) Macropulse average current vs integrated count per image in the region of interest. A linear behavior from 40 μA to 600 μA (b) Current transformer reading vs integrated counts on consecutive images for the four current settings.

using the average pixel value from outside the beam irradiation. This background region and region of interest (ROI) are annotated. An average beam current to CCD count dependence is shown in Fig. 9(a). Each data point corresponds to a current transformer reading and the corresponding image counts in the region of interest (ROI) for the given macropulse. There is a clear linear dependence between beam current and CCD counts. Figure 9(b) shows the temporal correlation of the beam transformer current and scaled CCD counts for ROI in the image for the same data as in Fig. 9(a).

D. Polarization study

The dominant component of transition radiation for a smooth target for low velocity beams is linearly polarized in the plane of radiation. This is one of the signatures of transition radiation in comparison to other photon inducing charged particle interactions like beam induced fluorescence (BIF) or material luminescence. We measured images for different polarizer settings with respect to the plane of observation for a macropulse containing 5×10^9 Ca^{10+} ion beam with velocity $\beta = 0.11$ irradiated on three target materials (aluminum, steel, and glassy carbon). One image was captured per macropulse. The multichannel plate (MCP) gain was set to 1.726 V. Figures 10 and 11 show 2D transverse profiles for $\psi = 20°$ at six consecutive polarizer angles from a steel and glassy carbon target, respectively. These images were obtained by averaging 250 images. The polarizer angle $= 120°$ is when the polarizer axis is parallel to the plane of observation. The number of CCD counts is generally factor ≈ 2 higher for the steel target in comparison to the glassy carbon target. There is a component that is polarized in the plane of observation for both steel and glassy carbon target. Observing linearly

polarized radiation from both metallic and dielectric targets can be considered evidence of OTR being a dominant radiation mechanism in vacuum for the given beam conditions. It is also worth noticing that in the case when the polarizer angle is perpendicular to the plane of observation (30°), there is still a significant amount of radiation left and the image corresponds well to the beam profiles with other polarizer settings. This can be understood as a consequence of the aforementioned surface roughness where the planes of radiation of microradiators do generally not coincide with one of the macroscopic targets. Therefore microradiators will effectively contribute to the photon yield which is unpolarized with respect to the plane of observation.

Figure 12(a) shows the average CCD counts for 250 images as a function of polarization for an irradiation angle of $\psi = 30°$ on an aluminum target. The polarizer angle was incremented in 30° steps for each set of measurements and covers the full 360°. For N image measurements under the same beam conditions, the error bar on the mean value of CCD counts is given by $\delta_{counts} = \sigma_{counts}/\sqrt{N}$. The polarization angles 120° and 300° correspond to the plane of observation. The counts are accumulated for three different regions of interest (ROIs). ROI 1 corresponds to the full image shown in Fig. 12(b). ROI 2 and 3 are marked in the figure. They were chosen to avoid the "hotspots" on the image. These hotspots occur at the same location on the target irrespective of beam movement, and therefore we suspect that they occur due to surface nonuniformity. The size of these hotspots is ascertained to be below 300 μm. However, the exact size of surface nonuniformities was not investigated post-irradiation. Their formation might have to do with larger local surface currents at these specific locations, resulting in larger photon yield. The counts from ROI 1 are scaled down by a factor of 10 for a better visualization. There is a good agreement with the
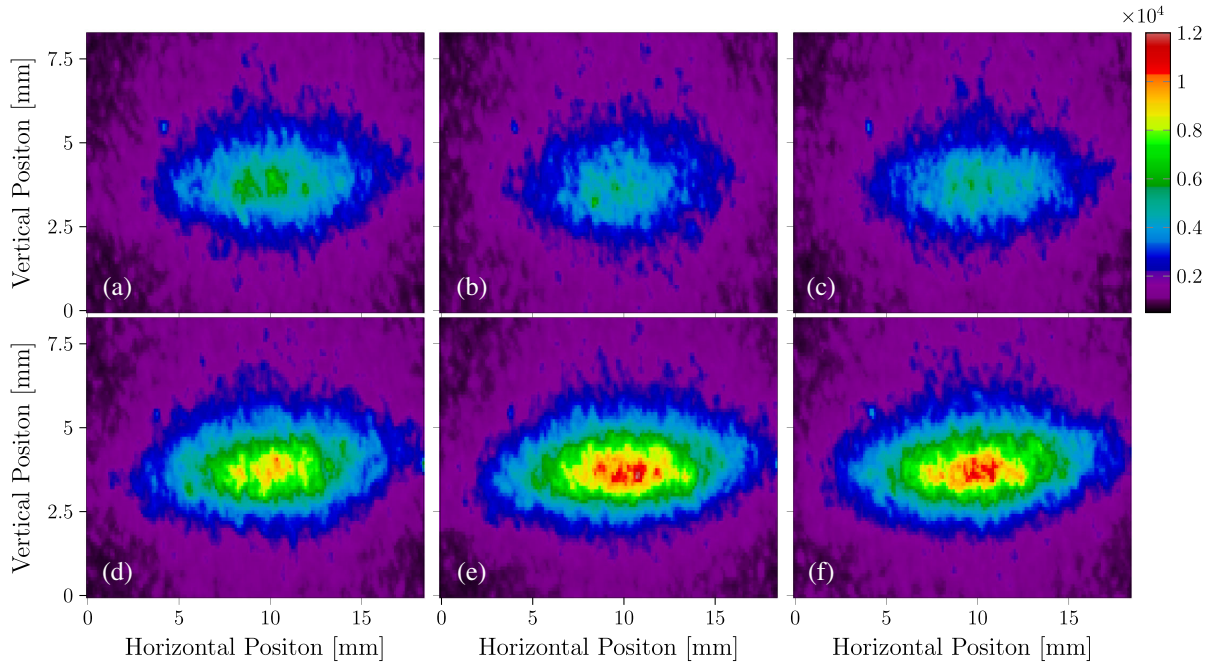
FIG. 10.   Image with a steel (V2A) target at 20° with respect to normal at the polarization angle of (a) 0°, (b) 30°, (c) 60°, (d) 90°, (e) 120°, and (f) 150°.

polarization curve for all ROIs; however, the best match is for ROI 2 which is the smallest of the three and devoid of any hotspots. However, there is seemingly no dependence on the relative contributions of polarized to unpolarized light to the choice of ROI. It is also worth noticing that in this specific case of aluminum for $\psi = 30°$, there is roughly a factor of ≈ 8 more unpolarized radiation compared to the

polarized component. The CCD images from the aluminum target for steep angles $\psi < 30°$ were saturated since many photons were registered in the few pixels of the CCD exposed in the vertical plane. In addition, the hotspots, as shown in Fig. 6 on the aluminum target, do not allow a quantitative comparison for different irradiation angles. We have therefore not considered the data from the aluminum
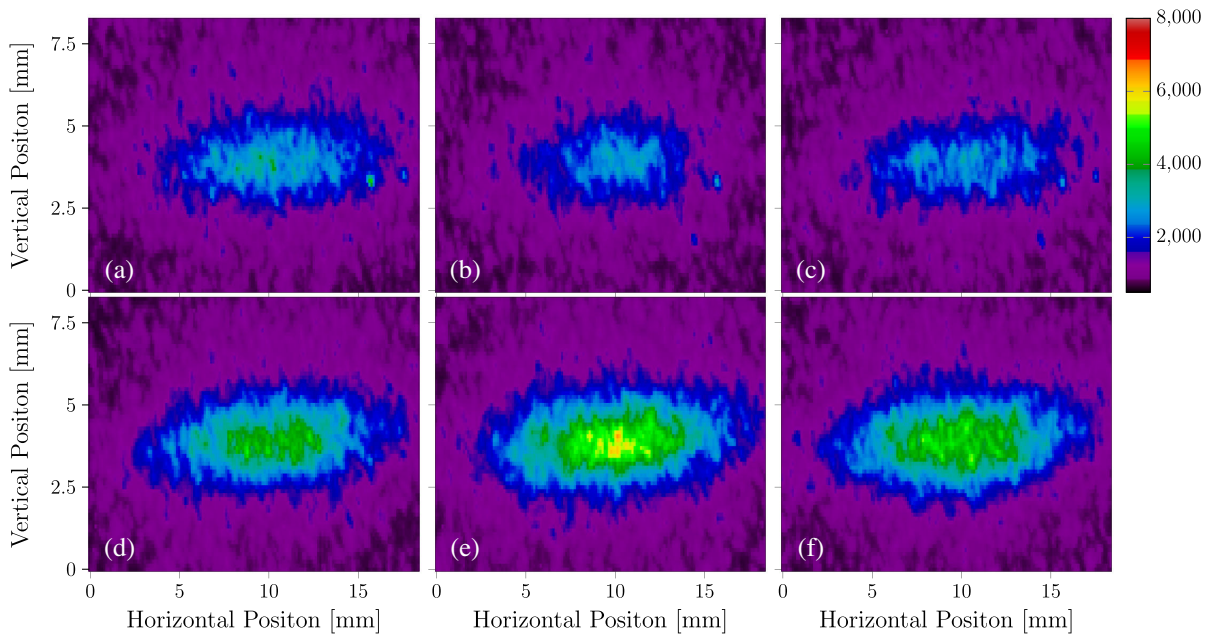

FIG. 11.   Image with a glassy carbon target at 20° with respect to normal at the polarization angle of (a) 0°, (b) 30°, (c) 60°, (d) 90°, (e) 120°, and (f) 150°.
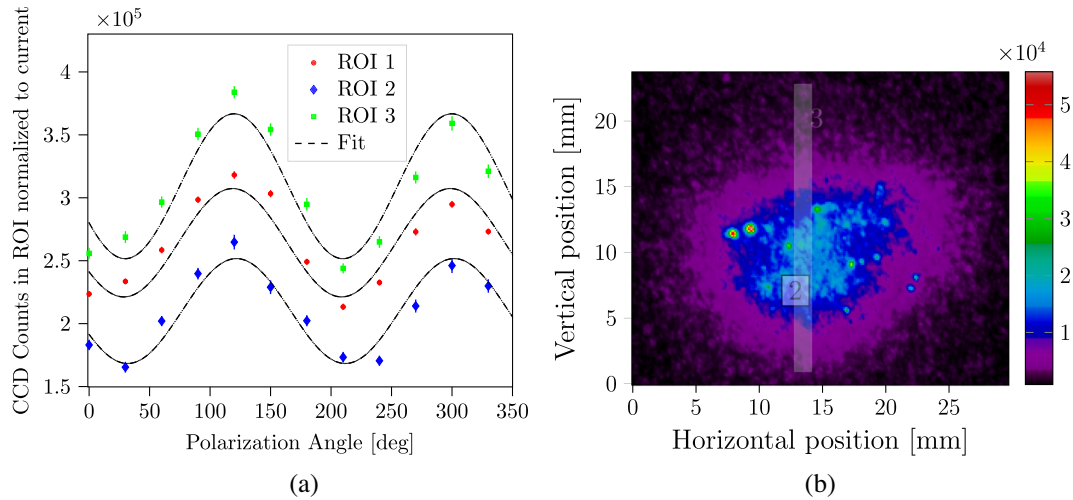
FIG. 12.   (a) OTR light output from an aluminum target as a function of polarizer angle. 120° and 300° on the polarizer corresponds to the plane of incidence. (b) The different regions of interest for calculated counts are shown in the image with hotspots due to the surface nonuniformities. ROI 1 corresponds to the shown full image while ROI 2 and ROI 3 are smaller sections as marked.

target for target rotation and angular distribution studies discussed in the following section. Further, we have observed that under heavy ion irradiation, the polarized components of radiation reduce over time while unpolarized component is unaffected. Faster surface deformation due to heavy ion irradiation might reduce the polarized contributions arising from $\vec{n}_{\mathrm{macro}}$ part of the target.

E. Light yield and angular distribution

Figures 10 and 11 show the images recorded at various polarizer angles for a fixed irradiation angle $\psi = 20°$. In the next step, we measured the radiation from several target angles in the range $\psi = 10°\text{–}70°$ along with a systematic variation in the polarizer settings covering 180° rotation in six steps. One has to note that the observation angle θ is correlated with irradiation angle $\theta = 90 - \psi$ when the

target is rotated. Figure 13 shows the CCD counts vs polarization angle for several irradiation angles for steel and glassy carbon targets. The CCD counts due to polarized photons and unpolarized photons can be separated by fitting the data with a typical polarization power curve. The peak intensity for most irradiation angles is seen at the polarizer angle of 120°, which is the angle when the polarizer axis coincides with the plane of observation. A peculiar observation is that at $\psi > 60°$, we see a shift in polarization direction and an emergence of polarization perpendicular to the plane of observation. The angle corrected transverse profiles are found to be consistent with each other.

In Fig. 14, we have summarized the linearly polarized and unpolarized radiation with respect to the plane of observation as a function of irradiation angles for steel and
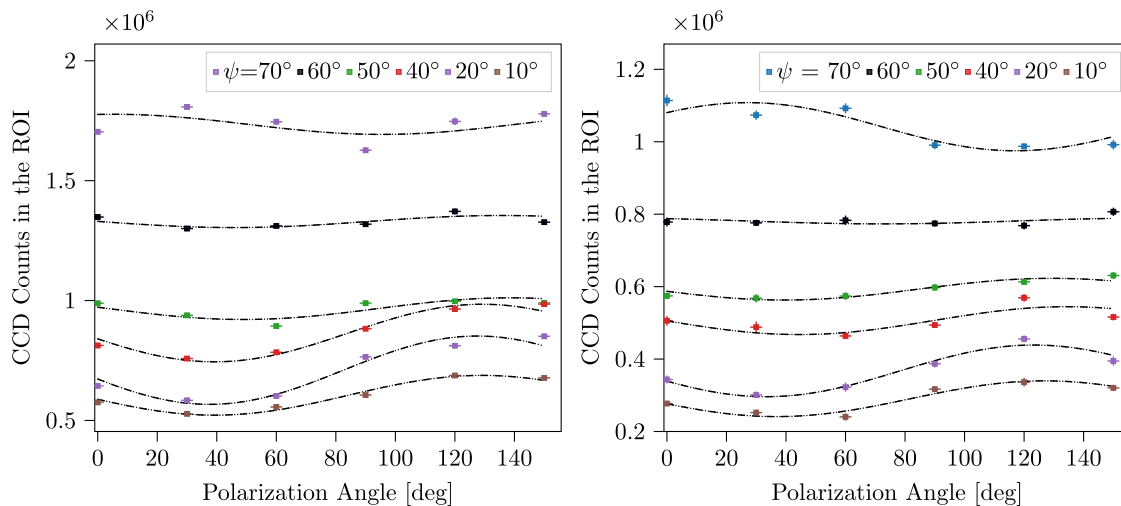

FIG. 13.   CCD counts as a function of incidence angle and polarization angle for steel target (left) and glassy carbon target (right).
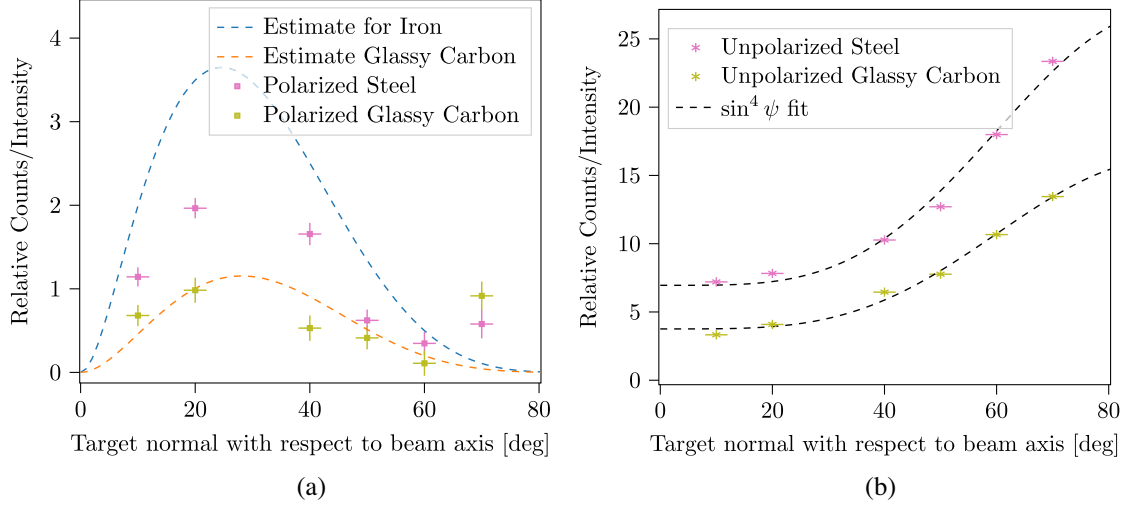
FIG. 14. (a) Detected polarized photons from steel (V2A) and glassy carbon target as a function of polarizer and target angle. (b) Unpolarized photons from steel (V2A) and glassy carbon target as a function of polarizer and target angle.

glassy carbon from the data shown in Fig. 13. The linearly polarized light in the observation plane is compared with the scaled theoretical estimate of photons shown in Fig. 5 as a function of ψ. The plots for the estimates are normalized to match the measured sample for glassy carbon at $\psi = 10°$. The polarized light is seen when the charges hit the surfaces whose normal vectors $\vec{n}_{\mathrm{micro,OTR}}$ coincide with the "macronormal" of the target $\vec{n}_{\mathrm{macro}}$. There is a good agreement for glassy carbon data. For the steel target, the trend against ψ is similar, but the absolute estimate value has a notable discrepancy. As mentioned earlier, the permittivity values for iron were used to estimate the theoretical light yield over irradiation angle to be compared to the steel target. One should note that the iron permittivity values available in the literature itself have a rather large variation [4,21].

The unpolarized component of radiation shown in Fig. 14(b) increases with ψ and could be fit satisfactorily with the lowest order dependence of $\sin^4\psi$. Similar observations were also made for gold and aluminum targets. The increase in photon counts at shallower angles (as $\psi \to \pi/2$) can be assigned to two categories of effects:

1. Geometrical factors

(i) One can expect that a certain proportion of generated photons from the micro-radiators will be scattered away from the detector by the structures on the target surface for normal incidence or steeper angles $\psi \to 0$. On the other hand, the surface scattering can direct additional photons (other than the ones in the line of sight toward the detector) toward the detector for grazing angles $\psi \to \pi/2$.

(ii) Significant radiation at grazing angles is directed toward the target surface which can be specularly reflected or scattered toward the detector resulting in an increase in light yield.

2. Modification of generation process

(i) The increase of the light yield toward grazing angles has been explained by diffraction radiation [16]. One should note that diffraction radiation drops exponentially as a function of ion distance from the surface [22], and the generation of any significant diffraction radiation can only happen when particles spend a lot of time close to the surface before hitting it.

(ii) There is also a possibility of the nonuniform surface features enhancing the transition radiation which can scale with the irradiated area. The basic mechanism would be similar to the one causing hotspots and higher radiation from edges.

It is difficult to distinguish the dominant component that results in the increased unpolarized radiation among all the effects discussed above. In another experimental observation, we observed a large amount of radiation when the edges of targets were irradiated. This could be explained by induction of large currents on edges resulting in higher OTR similar to the cause of hotspots due to local nonuniformity as discussed earlier.

Altogether, the aforementioned observations largely support our working hypothesis; i.e., a majority of the detected radiation on the CCD is indeed the modified optical transition or diffraction radiation due to the target surface roughness. The hypothesis is further strengthened by the measurements from the glassy carbon which is a radiation-hard dielectric material. The material properties of glassy carbon do not allow other generation mechanisms like surface plasmons and metallic oxide fluorescence. The yield for polarized, unpolarized, and background light scales expectedly with the permittivities of different target materials and hints strongly that all the radiation (including background) is primarily transition or diffraction radiation.
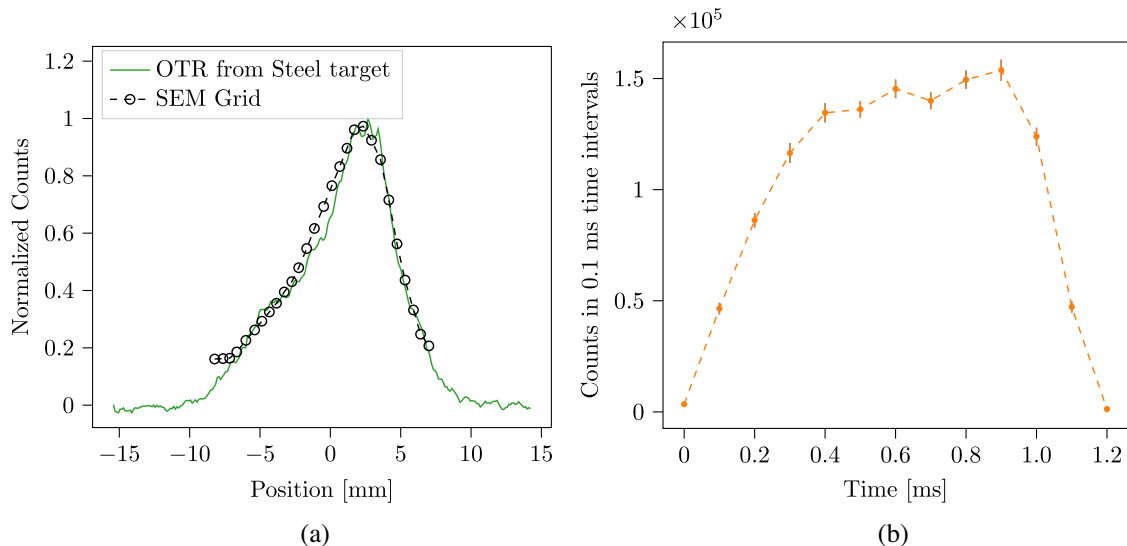
FIG. 15.   (a) Comparison of a horizontal profile from a secondary electron emission grid (SEM-Grid) and OTR light for an Ar^{18+} beam with 95 μA and 100 μs pulse length. (b) The mean count for Fe^{25+} beam with 20 μA average current in a 1 ms macropulse for 100 μs MCP gate width with a varying delay marked on the x-axis. The error bars are calculated from count fluctuations over 100 macropulses.

F. Comparison of OTR profile with SEM-Grid

A comparison between secondary electron emission monitor grid (SEM-Grid) and OTR image, which are longitudinally separated by 1 m, is shown in Fig. 15(a). This measurement was performed with an 8.6 MeV/u 95 μA Ar^{18+} beam irradiated on a steel target. The SEM-Grid wires are 2.1 mm apart and interpolation between the wires is performed by the SEM grid software. Generally, a good agreement between OTR images and SEM-Grid profiles is seen.

G. Counts as a function of MCP gate delay

As part of the initial studies to rule out fluorescence and any other slow processes, the MCP gate was set to a fixed width (100 μs) and the measurement was triggered at different delays with respect to beam macropulse arrival. This measurement was performed with an 11.4 MeV/u 20 μA Fe^{25+} beam with a macropulse length of 1 ms. The coarsely sampled pulse shape was reconstructed with this measurement in 13 delay steps as shown in Fig. 15(b).

H. Target heating and black body radiation

The number of OTR photons per image is in the order of 20–1000 for low intensity beams discussed in this report. Therefore profile imaging using OTR is sensitive to any black body radiation (BBR) visible regime resulting from target heating. An estimate of BBR per unit frequency f and solid angle Ω as a function of target temperature can be obtained by Planck's law,

$$\frac{dI_T(n,f)}{d\Omega df} = \frac{2hf^3}{c^2} \cdot \frac{1}{e^{hf/K_BT} - 1}. \tag{6}$$

Figure 16 shows the dependence of the number of photons generated as a function of target temperature for radiation centered in different parts of the spectra within 200 nm spectral width. One can see a threshold-like behavior, i.e., when the temperature of the target crosses a certain threshold, BBR with the longest wavelength allowed by the optical system will start to interfere with the measured profile image. As can be seen that already at 700 K temperature, photons centered at 500 nm photons can overwhelm the OTR based profile image. This behavior was observed with a 400 μA current Bi^{26+} beam on a steel target as shown in Fig 17(a). There was no optical filter applied for this specific measurement. Using a multichannel plate (MCP) gating
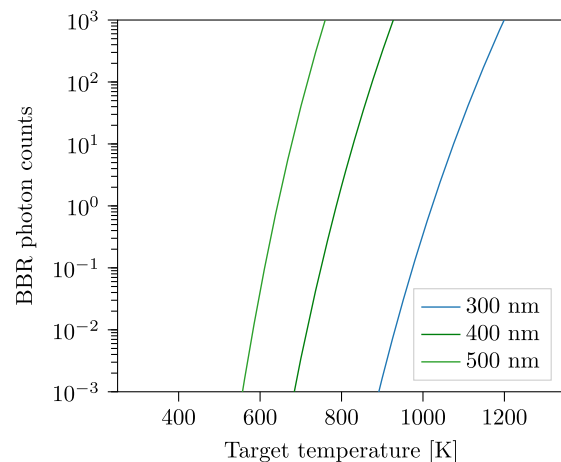

FIG. 16.   Black body radiation as a function of target surface temperature.
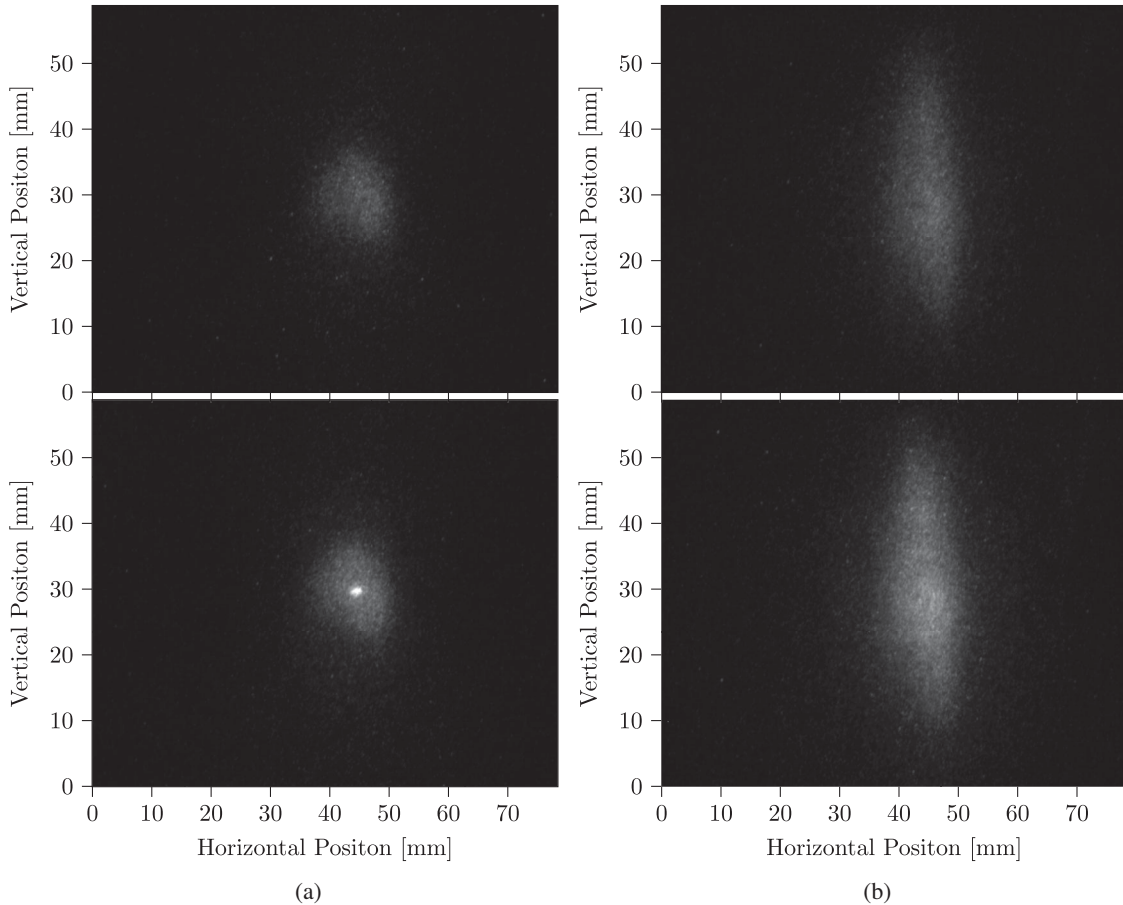
FIG. 17.   (a) Image with a 70 μs gate (top) and 100 μs (bottom) from the beginning of the macropulse for 400 μA current for target incidence $\psi = 25°$. (b) Image with a 70 μs gate (top) and 100 μs (bottom) from the beginning of the macropulse for 400 μA current for a target incidence of $\psi = 65°$.

period of 70 μs, the beam profile is not distorted while with a gate of 100 μs, the central part of the image is dominated by BBR. This led us to the conclusion that the center of the target crosses the temperature threshold at about 70 μs from the start the of macropulse. Target heating can be counteracted by depositing the beam energy of a larger surface area of the target as shown in Fig. 17(b), where under exactly the same beam conditions as Fig. 17(a), no BBR is observed. Since a larger area of the target was under irradiation, the target did not cross the temperature threshold to generate enough BBR. BBR can be reduced by utilizing shorter macropulses, shallower target angles, infrared filters, or active target cooling. Deducing from Fig. 16, the application of optical filters, which filter radiation longer than 300 nm, can allow the target temperature to increase up to 1100–1200K without any significant disturbance from BBR. For most practical measurements in our current range of up to few mA, target heating should not be an issue if macropulse length is controlled or an optical filter is applied. However, target heating always needs to be considered in OTR based diagnostics for low energy hadron beams.

IV. SUMMARY AND APPLICATIONS

We have shown that the OTR for ion beams provides enough photons for the measurement of a beam profile covering the typical range of intensities in accelerator operations. The light yield and polarization differ significantly between an ideal smooth target and the rough target as observed experimentally. A rough target has enhanced radiation at grazing angles, which can lower the intensity and energy thresholds for the usability of the OTR process in beam diagnostics. It also opens up possibilities for optimization of camera angles for beam imaging, nondestructive profile monitoring, and energy deposition on a larger surface area to avoid target heating. There are a few immediate applications, the first is the construction of a SEM-Grid like profiler for transversely small high intensity beams, since the construction of SEM-Grids is particularly challenging in those cases. The second use case is the modeling of nondestructive devices like ionization profile monitors (IPM) and beam induced fluorescence (BIF) monitors under high beam intensity. The IPM and BIF monitors are known to be affected by direct beam fields (space charge) and OTR can provide an *in-situ* nonspace

charge affected profile for correction and modeling. Finally, OTR with thin radiation hard materials like silicon carbide (SiC), glassy carbon, carbon stripper foils (already used at GSI [23]), zinc oxide (ZnO) in high energy beam transport opens up a possibility for an almost nondestructive profile monitoring, especially for fully stripped particles. The light yield after the synchrotrons should be high enough to be observed on a normal CCD directly.

Although the results presented in this paper are targeted at practical transverse profile measurement, there is still work to do toward theoretical modeling (in-line with [13]) at least for simpler surface structures [14] and experimental verification of the results as a function of surface roughness and irradiation angle on light yield. An evaluation of the precision of the profiles measured with the unpolarized component of the transition radiation in the context of scattering from rough surfaces and a detailed study of changes in the surface due to the effect of heavy ion bombardment is also required. This is relevant for detailed beam profile measurements for high intensity beams such as halo measurements or measurements of very narrow beams (<1 mm). There are other potential applications, e.g., if rough surfaces and multiple radiators could produce more than one photon per ion on an MCP for high energy beams; nondestructive OTR based particle spill counters during slow extraction can be foreseen similar to [24].

ACKNOWLEDGMENTS

APPENDIX A: CCD COUNT FLUCTUATIONS

An independent way of estimating the number of photons reaching the CCD is to evaluate the fluctuations in the number of counts for consecutive images under the same beam and target conditions during a stable machine operation.

There are three potential sources of CCD count fluctuations: (1) The first is due to the statistical fluctuation of the photon generation process. The fluctuations in discrete event generation are modeled by a Poisson process. For a Poisson process with an average of N events in a given time interval, the 1σ of the variation is expected to be $\sqrt{N}$. This is also referred to as "shot" noise in electronics literature. The second source of fluctuation is the MCP amplification process. It should be a constant for a given image intensifier setting and only weakly dependent on the number of amplified events. Another cause of CCD count fluctuations is the charged particle count fluctuations in consecutive macropulses.

Figure 18(a) shows the fluctuations in the CCD count for irradiation of the aluminum target for several incidence
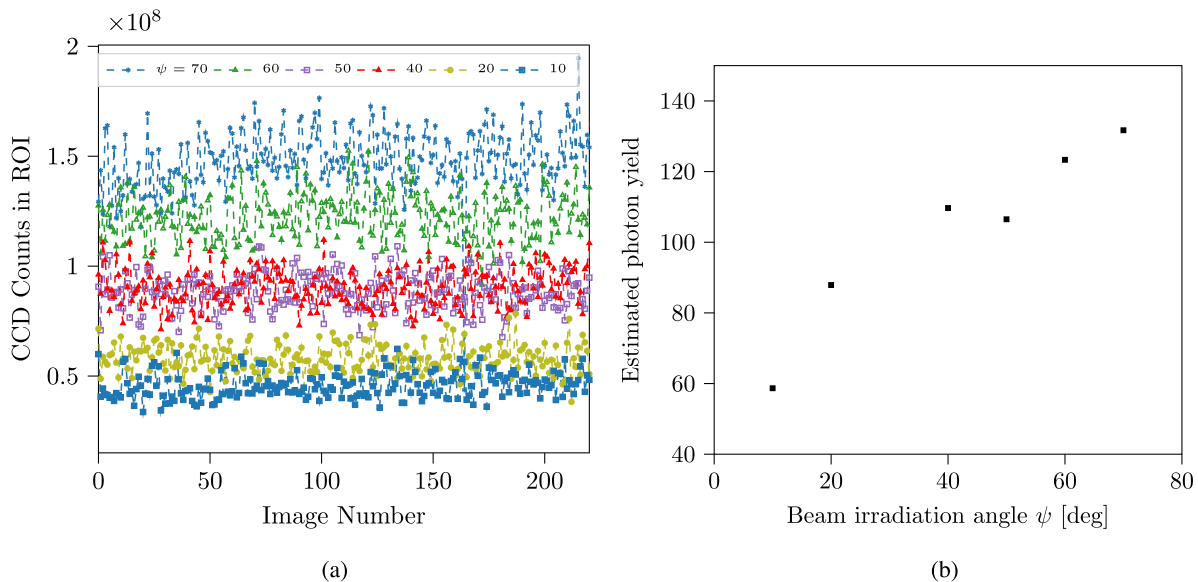

(a)

(b)

FIG. 18.   (a) CCD counts from aluminum target for various irradiation angles when the polarizer angle is set to 0°. (b) The number of average photons reaching the detector as a function of irradiation angle.

angles for a fixed image intensifier setting. Beam current is measured independently using a current transformer for each macropulse and was $40 \pm 1 \ \mu A$ for the presented data. The beam current fluctuations should contribute very weakly to the count fluctuations since $\frac{\sigma_I}{\langle I \rangle} \ll \frac{\sigma_{\mathrm{counts}}}{\langle \mathrm{counts} \rangle}$. There is a correlation in the average number of counts and its fluctuations, which hints that the fluctuation might be dominated by the photon generation process. Assuming that the fluctuation in count rates is dominated by the photon generation process, the average number of events or generated photons can be estimated as

$$N_{\mathrm{ph,average}} = \left(\frac{\langle \mathrm{counts} \rangle}{\sigma_{\mathrm{counts}}} \right)^2. \tag{A1}$$

The estimated photon counts from this procedure are shown in Fig. 18(b).

We have to note that the role of background subtraction is crucial for this process since this is an absolute photon number estimate. For $5 \times 10^9 \ Ca^{10+}$ beam with $\beta = 0.11$, we estimate the generation of 1000 photons for the aluminum target at $\psi = 30°$ (Fig. 5). The photocathode has an average quantum efficiency of 15%, and the optical

(a) Permittivity

(b) $\psi = 10°$
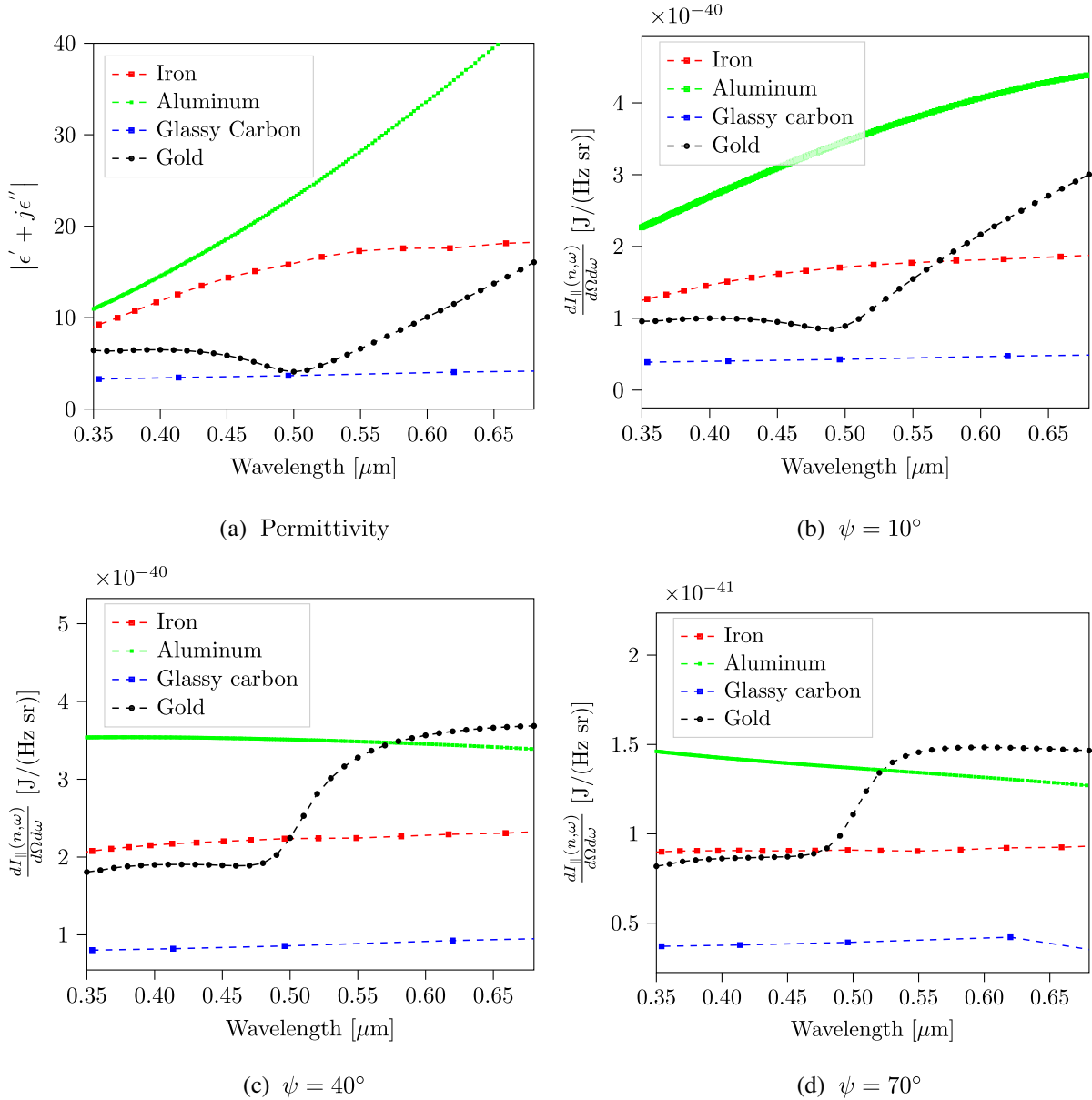
(c) $\psi = 40°$

(d) $\psi = 70°$

FIG. 19. Optical transition radiation spectra. (a) Shows the variation in absolute value of epsilon in visible range. (b–d) Calculated radiated intensity for different irradiation angles and the observation angle is $\theta = 90 - \psi$.

system should register a maximum of ≈150 photons per image from a smooth target. On the other hand, the photon estimate from the measurements is from a rough aluminum target, and the maximum intensity (140 photons) is measured at $\psi = 70°$. One should note that the data shown in Fig. 18 provides only a lower bound on the number of photons reaching the CCD. It is not distinguishable if the fluctuations are entirely driven by the TR generation process or if the noise in image intensification process also makes a contribution.

In comparison to photon yields above, the beam induced fluorescence monitor provides roughly ≈50 times lower number of photons when scaled for the same beam conditions [25]. About 500 events or photons are sufficient to provide a reliable 1D profile for an image intensified system if ≈10 bins are used in a histogram.

APPENDIX B: OTR SPECTRA

It is clear from Eq. (1) that the transition radiation spectral intensity is a rather complex function of material permittivity, angle of irradiation, and angle of observation. For low betas, e.g., ($\beta \ll 1$), it reduces to a simpler form.

$$\frac{dI_\parallel(n,\omega,\theta,\phi,\psi)}{d\Omega d\omega} = \frac{Z^2 e^2 \beta^2 \cos^2\psi}{4\pi^3 \epsilon_0 c} \left| \frac{\sin\theta \cos\theta(\epsilon-1)}{\epsilon \cos\theta + \sqrt{\epsilon - \sin^2\theta}} \right|^2 .$$
(A2)

The radiation intensity becomes low at the two extremes of observation angle θ due to $\cos\theta \sin\theta$ dependence. However, the effect of the material property on the spectra is easier to highlight close to these extremes. For a given irradiation angle ψ, as the angle of observation $\theta \to \pi/2$, the intensity $\frac{dI_\parallel(n,\omega)}{d\Omega d\omega} \approx |\epsilon - 1|$. Toward the other extreme as $\theta \to 0$, $\frac{dI_\parallel(n,\omega)}{d\Omega d\omega} \approx |\frac{\sqrt{\epsilon}-1}{\sqrt{\epsilon}}|^2$, which for sufficiently large values of ϵ approaches 1, will result in flattened spectra. Thus

depending on the angle of observation, the optical transition spectra may have the signature of the frequency dependence of the absolute value of permittivity. This is highlighted in Fig. 19, where the spectral intensity of the p-polarized component is shown for a particle with unit charge and velocity $\beta = 0.11$ and incident on the target materials aluminum, iron, gold, and glassy carbon. We should note that the observation angle in Fig. 19 is a function of irradiation angle $\theta = 90 - \psi$ in compliance with the rest of the manuscript and our experimental setup. The frequency dependence of permittivity values is acquired from [4,26,27].

APPENDIX C: EXPECTED PHOTON NUMBER FOR PEC AT NORMAL INCIDENCE

Setting $\epsilon = 10^{12}$ (to emulate a perfect electric conductor) and $\psi = 0$, we can compare photon number (4) derived from spectral intensity (1) for an oblique case with the result obtained using spectral energy ([2])

$$\frac{dE}{d\omega} = \frac{Z^2 e^2}{4\pi^2 \epsilon_0 c} \left(\frac{1+\beta^2}{2\beta} \ln\left(\frac{1+\beta}{1-\beta}\right) - 1 \right), \quad (A3)$$

which is valid for normal incidence and PEC. In the latter case, the total photon number is given as

$$N_{\text{ph,PEC},\perp} = \frac{N_{\text{ion}}}{\hbar} \ln\left(\frac{\omega_2}{\omega_1}\right) \frac{dE}{d\omega}. \quad (A4)$$

For $N_{\text{ion}} = 5 \times 10^9$ ions with charge state $Z = 10$ traveling with $\beta = 0.11$ and in the wavelength range $\lambda \in [350, 650]$ nm, one obtains 1.166×10^7 photons using (A4). This gives a scaling of $N_{\text{ph},t} = 2 \times 10^{-3} \beta^2 Z^2 N_{\text{ions}}$ in-line with Eq. (5).
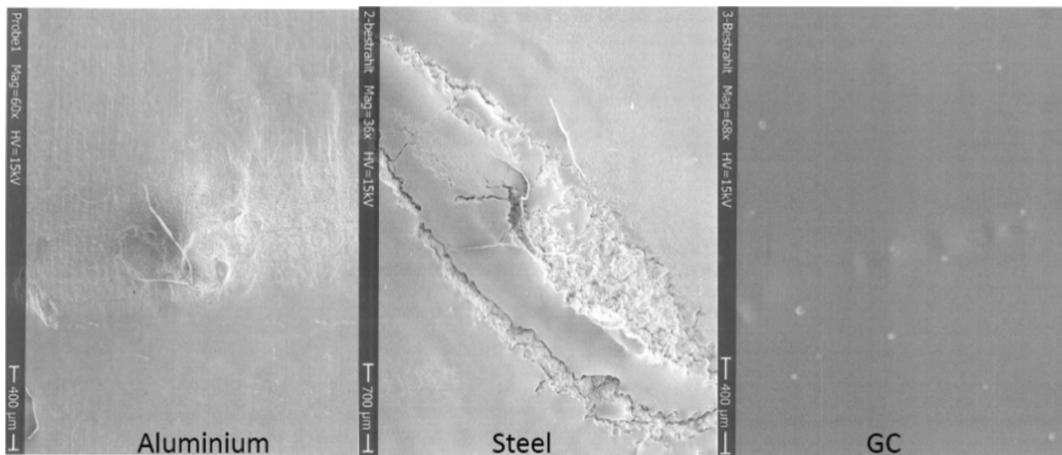

FIG. 20.   Photos of the irradiated target areas after 8 h of beam irradiation. The scale is marked on the lower left of each image.
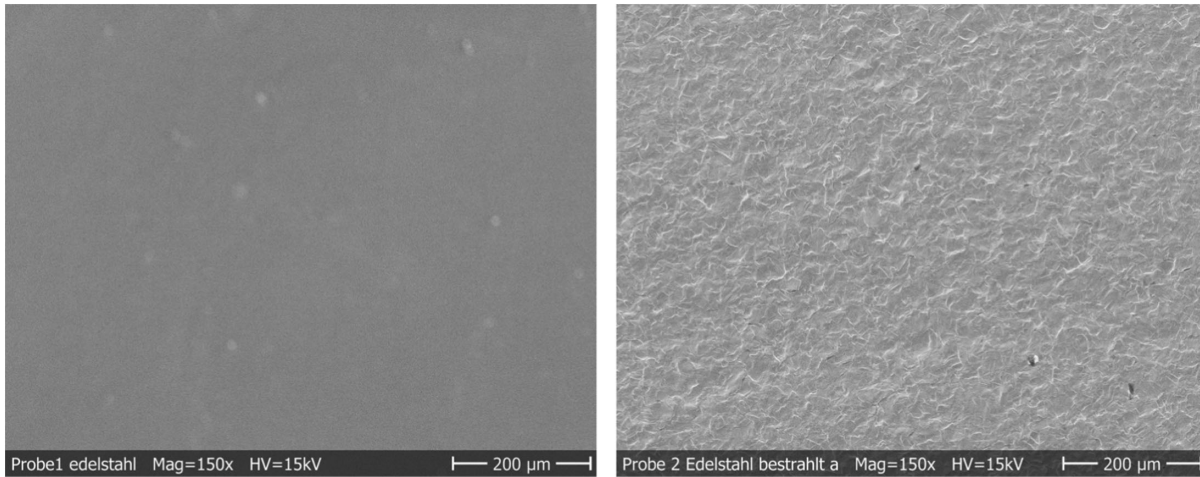
FIG. 21.   Left: nonirradiated part of steel target. Right: irradiated part of steel target.

APPENDIX D: POST-IRRADIATION TARGET SURFACES

The OTR targets were analyzed after irradiation in terms of surface distortion and chemical composition and compared between irradiated and nonirradiated areas of the target. The characterization was performed using scanning electron microscope with energy dispersive x-ray spectroscopy analysis. The chemical composition did not change due to irradiation. The steel and glassy carbon targets were relatively uniform in nonirradiated area while there were several nonuniformities of ≈ 1.5 μm were observed on aluminum targets (see Table I below). The images of target center after 8 h of irradiation with Ar^{10+} 50 μA beam are shown in Fig. 20. Each sample was irradiated with a maximum of 25,000 macropulses of 1 ms each. The aluminum and steel surfaces have a visible distortion while glassy carbon target seemed unaffected visually. Figure 21 shows a higher resolution comparison of the steel target between irradiated and nonirradiated area under a "moderate" irradiation of 50 consecutive macropulse irradiation of 100 us each. The surface roughness factor R_a is measured using the surface roughness line profiler Taylor-Hobson Surtronic 3+. The length of profile over which R_a is measured is 0.8 mm and five readings are taken close to irradiation center as well as outside the irradiation center for each case.

TABLE I.   The surface roughness inside and outside the irradiation area.

Target	Outside	Inside
Aluminum	0.28 ± 0.1	2.5 ± 0.3
Long irradiated steel	0.16 ± 0.06	13.4 ± 0.2
Moderate irradiated steel	0.16 ± 0.06	0.9 ± 0.1
Glassy carbon	0.06 ± 0.02	0.24 ± 0.06

The results are shown in Table I. The measurements exactly at the center of the steel target were prohibited due to significant damage and the measurement range of the line profiler.

[1] V. L. Ginzburg and I. M. Frank, Transition radiation, Zh. Eksp. Teor. Fiz. **16**, 15 (1946).

[2] V. L. Ginzburg and V. N. Tsytovich, *Transition Radiation and Transition Scattering* (Adam Hilger, New York, 1990).

[3] M. Ter-Mikaelian, *High Energy Electromagnetic Processes in Condensed Media* (Wiley/Interscience, New York, 1972).

[4] P. B. Johnson and R. W. Christy, Optical constants of transition metals: Ti, V, Cr, Mn, Fe, Co, Ni, and Pd, Phys. Rev. B **9**, 5056 (1974).

[5] C. Bal, E. Bravin, E. Chevallay, T. Lefevre, and G. Suberlucq, OTR from non-relativistic electrons, in *Proceedings of the 6th European Workshop on Beam Diagnostics and Instrumentation for Particle Accelerators, Mainz, Germany, 2003* (JACoW Publishing, Geneva, Switzerland, 2003), https://accelconf.web.cern.ch/d03/papers/PM04.pdf.

[6] R. B. Fiorito, D. Feldman, A. G. Shkvarunets, S. Casey, B. L. Beaudoin, B. Quinn, and P. G. O'Shea, OTR measurements of the 10 kev electron beam at the University of Maryland electron ring (UMER), in *Proceedings of the 22nd Particle Accelerator Conference, PAC-2007, Albuquerque, NM* (IEEE, New York, 2007), pp. 4006–4008.

[7] A. Lumpkin, Feasibility of OTR imaging of non-relativisitc ions at GSI, in *Proceedings of the 24th Particle Accelerator Conference, PAC-2011, New York, 2011* (IEEE, New York, 2011).

[8] B. Walasek-Hoehne *et al.*, Pilot studies on optical transition radiation imaging of non-relativistic ions at GSI, in *Proceedings of the 15th Beam Instrumentation Workshop (BIW'12) Newport News, VA, 2012* (JACoW Publishing, Geneva, Switzerland, 2012), paper TUCP03, pp. 130–132, https://jacow.org/ BIW2012/papers/TUCP03.pdf.

[9] B. Walasek-Höhne, C. Andre, F. Becker, P. Forck, A. Reiter, M. Schwickert, and A. Lumpkin, Optical transition radiation for non-relativistic ion beams, in *Proceedings of the High-Intensity and High-Brightness Hadron Beams, Beijing, China, 2012* (JACoW, Geneva, 2012), paper THO3C01, p. 580.

[10] A. A. Maradudin and E. R. Mendez, Light scattering from randomly rough surfaces, Sci. Prog. **90**, 161 (2007).

[11] V. Verzilov, Transition radiation in the pre-wave zone, Phys. Lett. A **273**, 135 (2000).

[12] R. Singh and T. Reichert, Longitudinal charge distribution measurement of non-relativistic ion beams using coherent transition radiation, Phys. Rev. Accel. Beams **25**, 032801 (2022).

[13] R. A. Bagiyan, Transition radiation from rough surfaces, Acta Phys. Superficierum **2**, 13 (1990).

[14] J. E. Rutkowski, Transition radiation emitted from a surface irregularity shaped as rectangular step and rectangular groove, Acta Phys. Superficierum **2**, 59 (1990).

[15] G. M. Garibyan, Transition radiation effects in particle energy, J. Exp. Theor. Phys. (U.S.S.R.) **37**, 527 (1959), http://www.jetp.ras.ru/cgi-bin/dn/e_050_05_0895.pdf.

[16] F. R. Arutyunyan, A. Kh. Mkhitaryan, R. A. Oganesyan, B. O. Rostomyan, and M. G. Sarinyan, Polarization and spectral composition of the radiation of nonrelativistic electrons interacting with a rough surface, Zh. Eksp. Teor. Fiz. **77**, 1788 (1979), http://jetp.ras.ru/cgi-bin/dn/e_010_02_0372.pdf.

[17] C. Reid, Measurement of electron beam emittance using optical transition radiation and development of a diffuse screen electron beam monitor, NPS thesis, 1990.

[18] H. Boersch, P. Dobberstein, D. Fritzsche, and G. Sauerbrey, Transition Radiation, Bremsstrahlung und Plasmastrahlung, Z. Phys. **187**, 97 (1965).

[19] L. S. Cram and E. T. Arakawa, Bremsstrahlung and transition radiation from Ag foils bombarded by non-normal incidence electrons, Phys. Rev. **153**, 455 (1967).

[20] https://www.gsi.de/work/beschleunigerbetrieb/beschleuniger/unilac/unilac.

[21] M. A. Ordal, L. L. Long, R. J. Bell, S. E. Bell, R. R. Bell, R. W. Alexander, Jr., and C. A. Ward, Optical properties of the metals Al, Co, Cu, Au, Fe, Pb, Ni, Pd, Pt, Ag, Ti, and W in the infrared and far infrared, Appl. Opt. **22** (1983).

[22] A. Cianchi, M. Castellano, L. Catani, E. Chiadroni, K. Honkavaara, and G. Kube, Nonintercepting electron beam size monitor using optical diffraction radiation interference, Phys. Rev. ST Accel. Beams **14**, 102803 (2011).

[23] W. Barth, M. S. Kaiser, B Lommel, M. Maier, S. Mickat, B. Schlitt, J. Steiner, M. Tomut, and H. Vormann, Carbon stripper foils for high current heavy ion operation., J. Radioanal. Nucl. Chem. **299**, 1047 (2014).

[24] J. Bosser, J. Mann, G. Ferioli, and L. Warstki, Optical transition radiation proton beam profile monitor, Nucl. Instrum. Methods Phys. Res., Sect. A **238**, 45 (1985).

[25] C. Andre, P. Forck, R. Haseitl, A. Reiter, R. Singh, and B. Walasek-Hoehne, Optimization of beam induced fluorescence monitors for profile measurements of high current heavy Ion beams at GSI, in *Proceedings of IBIC2014, Monterey, CA* (JACoW Publishing, Geneva, Switzerland, 2014), paper TUPD05, https://jacow.org/IBIC2014/papers/TUPD05.pdf.

[26] M. W. Williams and E. T. Arakawa, Optical properties of glassy carbon from 0 to 82 eV, J. Appl. Phys. **43**, 3460 (1972).

[27] F. Cheng, P.-H. Su, J. Choi, S. Gwo, X. Li, and C.-K. Shih, Epitaxial growth of atomically smooth aluminium on silicon and its intrinsic optical properties, ACS Nano **10**, 9852 (2016).